



## City Research Online

### City, University of London Institutional Repository

---

**Citation:** Bellini, R., Rodriguez, C., Karathanassis, I. K., Pickett, L., Gavaises, M. & Geber, E. (2024). Modelling of wall-bounded cavitating flow and spray mixing in multi-component environments using the PC-SAFT equation of state. *Applications in Energy and Combustion Science*, 20, 100295. doi: 10.1016/j.jaecs.2024.100295

This is the published version of the paper.

This version of the publication may differ from the final published version.

---

**Permanent repository link:** <https://openaccess.city.ac.uk/id/eprint/33863/>

**Link to published version:** <https://doi.org/10.1016/j.jaecs.2024.100295>

**Copyright:** City Research Online aims to make research outputs of City, University of London available to a wider audience. Copyright and Moral Rights remain with the author(s) and/or copyright holders. URLs from City Research Online may be freely distributed and linked to.

**Reuse:** Copies of full items can be used for personal research or study, educational, or not-for-profit purposes without prior permission or charge. Provided that the authors, title and full bibliographic details are credited, a hyperlink and/or URL is given for the original metadata page and the content is not changed in any way.

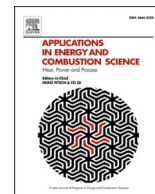
---

City Research Online:

<http://openaccess.city.ac.uk/>

[publications@city.ac.uk](mailto:publications@city.ac.uk)

---



## Modelling of wall-bounded cavitating flow and spray mixing in multi-component environments using the PC-SAFT equation of state

R. Bellini<sup>a,\*</sup>, C. Rodriguez<sup>a,\*</sup>, I.K. Karathanassis<sup>a</sup>, L. Pickett<sup>b</sup>, M. Gavaises<sup>a</sup>, E. Geber<sup>a</sup>

<sup>a</sup> School of Science & Technology, City, University of London, Northampton Square, London EC1V 0HB, UK

<sup>b</sup> Combustion Research Facility, Sandia National Laboratory, 7011 East Ave, Livermore 94550, CA, United States

### ARTICLE INFO

#### Keywords:

Two-phase numerical model  
Phase-change  
Fuel injection  
Spray atomisation  
Diffuse-interface approach  
PC-SAFT

### ABSTRACT

This work introduces a numerical multiphase model for multi-component mixtures, utilizing tabulated data for physical and transport properties across a spectrum of conditions from near-vacuum pressures to supercritical states. The property data are derived using Perturbed Chain Statistical Associating Fluid Theory (PC-SAFT), vapor-liquid equilibrium (VLE) calculations, entropy scaling methodologies, and Group Contribution (GC) methods. These techniques accurately reflect the thermodynamic behaviors of real fluids, avoiding the empirical estimation of Equation of State (EoS) input parameters. Implemented in OpenFOAM, the fluid dynamics solver is designed to address the three-dimensional Navier-Stokes equations for multi-component mixtures. The methodology integrates operator splitting to manage hyperbolic and parabolic steps distinctively. Hyperbolic terms are solved using the HLLC (Harten-Lax-van Leer-Contact) solver with temporal integration performed via a third-order Strong-Stability-Preserving Runge-Kutta (SSP-RK3) method. Viscous stress tensor contributions in the momentum equation are handled through an implicit velocity correction equation, while parabolic terms in the energy equation are explicitly solved. The simulation efficiency is further enhanced by adaptive Local Time Stepping and the Immersed Boundary (IB) method, which addresses interactions between the fluid and solid boundaries. Turbulence is resolved using the Wall Adaptive Large Eddy (WALE) model. Applied to high-pressure diesel fuel spray injections into non-reacting (nitrogen) gas environments, the model has been validated against Engine Combustion Network (ECN) data for the Spray-C configuration, featuring a fully cavitating multi-hole orifice. Results demonstrate that the model achieves accurate predictions across a broad range of tested conditions without the need for tuning or calibration parameters.

### 1. Introduction

Utilization of net zero CO<sub>2</sub> emission (NZE) and/or carbon-free fuels and relevant infrastructure [59] are developing fast and are gradually becoming a reality. Still, fossil-fuel based energy and transportation power systems currently count ~23 % of energy consumption globally, while they are expected to double over the next 2 decades due to increased commerce and movement of goods across oceans, nations, and cities [17]. The expected increase in fuel demand will be mainly consumed by off-road, heavy duty and marine Diesel engines. Reduction of emissions from such combustion engines strongly depends on the efficient design of advanced fuel injection equipment, widely accepted as a key industrial priority for >30 years [64]. The development of high-pressure common rail systems in particular, initially introduced to the market in 1997, has resulted to ~50 % reduction in NO<sub>x</sub> and soot

alone, irrespectively of the emission after-treatment technology utilised; such systems are now almost exclusively used in most vehicle types. This reduction of emissions is due to enhanced mixing achieved by the increasing injection pressure beyond 2000 bar, which enhances the atomisation of the injected fuel and thus, reduces vaporisation time. Along these lines, significant reduction of emissions can be achieved by injecting fuel against air charge being at pressure & temperature (P-T) conditions well above the fuel's critical point, since that reduces the fuel heating time and results to enhanced air-fuel mixing at conditions associated with the disappearance of the liquid-gas phase boundary, as in supercritical fluid conditions [1,45]. Utilisation of NZE fuels, biofuels and relevant additives could lead to a further decrease in soot formation during combustion in all types of internal combustion engines [5,29,36,42]; at the same time, multiple injections of short duration that modulate the fuel delivery via the fast opening/closing of the injector's needle valve and exhaust gas recirculation can significantly reduce both soot

\* Corresponding authors.

E-mail addresses: [raffaele.bellini.2@city.ac.uk](mailto:raffaele.bellini.2@city.ac.uk) (R. Bellini), [carlos.rodriguez@city.ac.uk](mailto:carlos.rodriguez@city.ac.uk) (C. Rodriguez).

<https://doi.org/10.1016/j.jaecs.2024.100295>

Received 1 June 2024; Received in revised form 11 September 2024; Accepted 27 September 2024

Available online 1 October 2024

2666-352X/© 2024 The Authors. Published by Elsevier Ltd. This is an open access article under the CC BY license (<http://creativecommons.org/licenses/by/4.0/>).

**Nomenclature***List of abbreviations*

AAD	Average Absolute Deviation
CFL	Courant–Friedrichs–Lewy
ECN	Engine Combustion Network
EoS	Equation of State
GC	Group Contribution
HLLC	Harten-Lax-van Leer-Contact
PR	Peng-Robinson
PC-SAFT	Perturbed Chain Statistical Associating Fluid Theory
SSP-RK3	Third-order Strong-Stability-Preserving Runge–Kutta
TPn flash	Isothermal-Isobaric Flash
TVD	Total Variation Diminishing
TPD	Tangent Plane Distance
VLE	Vapor-Liquid Equilibrium

*List of Symbols*

$\tilde{a}^{res}$	Reduced Helmholtz free energy [-]
$c$	Speed of sound [ $\text{m s}^{-1}$ ]
$d$	Temperature-dependent segment diameter [ $\text{\AA}$ ]
$e$	Internal energy [ $\text{J mol}^{-1}$ ]
$h$	Enthalpy [ $\text{J mol}^{-1}$ ]
$g$	Gibbs energy [ $\text{J mol}^{-1}$ ]
$I$	Integrals of the perturbation theory [-]
$k_b$	Boltzmann constant [ $\text{J K}^{-1}$ ]
$m$	Number of segments per chain [-]
$\bar{m}$	Mean segment number in the system [-]

$M_M$	Molecular weight [ $\text{g mol}^{-1}$ ]
$N_A$	Avogadro's number [ $\text{mol}^{-1}$ ]
$p$	Pressure [Pa]
$p_c$	Critical pressure [Pa]
$R$	Gas constant [ $\text{J mol}^{-1} \text{K}^{-1}$ ]
$T$	Temperature [K]
$T_c$	Critical temperature [K]
$x_i$	Mole fraction of component $i$ [-]
$w$	Acentric factor [-]
$Z$	Compressibility factor [-]

*Greek Letters*

$\beta$	Overall fraction of vapour phase [-]
$\varepsilon$	Depth of pair potential [J]
$\rho$	Density [ $\text{kg/m}^3$ ]
$\rho_m$	Total number density of molecules [ $1/\text{\AA}^3$ ]
$\sigma_d$	Segment diameter [ $\text{\AA}$ ]
$\theta$	Vapour volume fraction [-]
$\varphi$	Fugacity coefficient [-]
$\mu$	Chemical potential [ $\text{J mol}^{-1}$ ]

*Superscripts*

$EQ$	Equilibrium
$disp$	Contribution due to dispersive attraction
$hc$	Residual contribution of hard-chain system
$hs$	Residual contribution of hard-sphere system
$id$	Ideal gas contribution

and NOx emissions, as demonstrated long ago [27]. Relevant to the present work, experimental data have shown that increasing the injection pressure even up to 500 MPa will cause a reduction in soot formation [57,62,94]. The latter detailed experimental work analyzed the behavior of the evaporation, mixing, and combustion, revealing the improved mixing due to higher spray velocities. However, the  $\mu\text{m}$ -scale of injectors makes experimental flow characterization inside the injector challenging, especially under such high injection pressures. Increasing the injection pressure and multiple injections of short duration results in very high fuel velocities combined and in-nozzle fuel temperature increase [95] as recently reported by the authors. At such transient and elevated rail pressure conditions, the sharp pressure and temperature gradients lead to formation of cavitation that cannot be compensated by tapered nozzles. Although cavitation collapse may remove surface deposits and improve primary jet break-up [83], it may also damage the injector material [15,54,101] and reduce the injector's fuel delivery capacity.

As experimentation at such conditions is rather limited, the vast majority of studies relevant to fuel injection utilise CFD models, which have found applications in this field for >30 years. Early studies developed since the mid '80 s that have decoupled the in-nozzle flow phase-change effects from the subsequent atomisation/mixing of the injected fuel, despite the fact that they are strongly linked together, still represent the most frequently used assumption when it gets to industrial design; this is due to the fact that flow methodologies adopting a fully-coupled multi-scale and multi-physics approach coupling the in-nozzle flow development with the fuel atomisation and further mixing are computationally demanding. The well-known Eulerian-Lagrangian approach for modelling the spray development utilises as inlet/boundary conditions information relevant to the fuel injection rate. The latter can be either predicted or measured. The first attempt of a phenomenological model introduced to capture the effects on in-nozzle cavitation on spray formation has been reported in [3]. Subsequent but still early studies have utilised the volume of fluid (VOF) model to simulate

simultaneously the in-nozzle flow and the subsequent spray development, but for non-cavitating nozzle configurations and assuming fixed fuel properties. Probably the first works addressing the strong dependence of fuel properties on pressure and temperature via real fluid thermodynamics effects in fuel injection are those from the author's group [87]; still, only in-nozzle flow simulations using RANS were employed, which has greatly under-resolved turbulence effects and without linking to subsequent spray formation. The detrimental effect of turbulence in Diesel injector operation has been analysed in [73], showing the generation of highly transient cavitation structures that can travel even beyond the orifice exit, affecting the injected spray. Numerical works trying to compute the in-nozzle flow simultaneously with the jet/spray formation have only recently appeared. In [14] a multi-level simulation of a Diesel injector was performed. The flow distribution at the injector outlet was subsequently used for spray modelling inside the engine cylinder; while this enabled the prediction of the jet, coupling between jet and in-nozzle flow was weakly enforced in a one-way manner. The numerical work of [61] on Diesel injectors involved a stronger coupling of in-nozzle flow and jet atomisation in a unified framework; however, the thermodynamic model omitted temperature dependence effects. The author's works of [21,77] have utilised barotropic-type models for simulating simultaneously and in a fully-coupled manner the in-nozzle flow, nozzle wall wetting, fuel dripping and the spray formation but for low injection pressure conditions which does not require the strong variation of fuel properties with P-T to be taken into account. Recent works [11] have investigated the effect of cavitation and fuel properties on nozzle flow, spray formation and induced erosion in fuel injectors. Still, in these studies although an Eulerian-Eulerian two-fluid model was utilised in AVL Fire, a weak coupling between the in-nozzle flow and the subsequent spray was imposed by splitting the computational domain at the injector exit and performing separate simulations for the in-nozzle flow and the subsequent spray formation.

These fully-coupled in-nozzle flow and spray evolution simulations

are not applicable under supercritical fluid conditions (SFC) in fuel injection, which are promising to increase engine performance while reducing emissions [13,18,63]. Investigations of the critical data of Diesel fuel and its components were recently reported in [46] showing enlarged cone angles and improved mixing. An inherent advantage of SFC injection is the absence of the enthalpy of vaporisation and the low (or zero) surface tension. This is observed whether the SFC fuel is a single-component, a surrogate fuel or a more realistic, multi-component mixture [2]. One limitation in studying SFC injection is the absence of databases for the fuel's properties over the extreme P-T conditions required. The recently published database for Diesel surrogates from Sandia National Labs [55], specifically derived for overcoming the uncertainties in relevant modelling activities, is limited to conditions below the fuel's critical point. NIST databases [43] include hydrocarbon's data from methane only up to dodecane (C12); however Diesel composition involves hydrocarbons up to n-docosane (C22), for which data are missing. Since Diesel fuel is a complex hydrocarbon mixture, one needs not only the properties of the components but mixing relations that depart from idealised thermodynamics [28]. As NIST or other databases are not applicable, it is commonplace to either employ an advanced cubic Equation of State (EoS) [40] with relevant mixing rules [52] or employ a semi-empirical Helmholtz energy model (PC-SAFT) [4]. The problem is that, due to the complexity of the phase diagram, even advanced cubic EoS may not be accurate enough. Thus, modifications/improvements have been developed to improve accuracy of EoS, e.g. the "Volume Translation" method for the Peng-Robinson (PR) and Soave-Redlich-Kwong [51]. Especially for heavy hydrocarbons, measurements are limited up to 523 K [100], which is  $\sim 130$  K lower than the critical point, necessitating additional measurements describing critical conditions for Diesel fuel blends, including bio-fuels. Recently, new experiments and simulations on the properties of diesel fuel at elevated pressures and temperatures have been performed, see selectively for pressures up to 450 MPa [69,71,96]. Relevant to this study, the thermophysical properties, such as density and viscosity, were modelled by the author's team, using the PC-SAFT theory for pressures up to 450 MPa [95]. Tabulated data were derived for various fuel surrogates covering the range of properties occurring within high pressure fuel injectors, and thus allowing for an accurate estimation of the effects of the various fuel properties to be considered. Such data have been also used for coupling the in-nozzle flow with spray simulations in recent studies, but without considering cavitation [38], or by using a simplified mass transfer rate cavitation model [93].

Novel methodologies utilising implicit pressure-based finite-volume frameworks, incorporating real-fluid equations of state (EoS), multi-component vapor-liquid equilibrium (VLE) calculations [38], and diffuse interface methodologies have been presented recently. However, these face difficulties in achieving convergence when dealing with internal flows under cavitating conditions. This difficulty stems from the representation of density as a function of pressure and temperature, leading to a discontinuous density field that makes the implicit iterative solution unstable. In a study of [52], it was shown that an explicit multiphase, density-based, large-eddy Eulerian model can be utilized to simulate liquid-fuel injection and mixing under high-pressure conditions. The model incorporates the PR equation of state and vapor-liquid equilibrium calculations. To identify single-phase and two-phase states, an isobaric-isothermal algorithm (PT-flash) and a Tangent Plane Distance (TPD) function are employed. In the case of a two-phase state, the PT-flash algorithm determines the composition of the liquid and vapor phases by minimizing the Gibbs free energy of the system. This approach yielded precise results for the baseline case of the ECN Spray A fuel injector [74] under various operating conditions. In [20], the CFD approach described in [52] was employed along with an optimised isoenergetic-isochoric algorithm (UV-flash) [19] to simulate both inert and reactive sprays under trans-critical conditions. The Redlich-Kwong-Peng-Robinson (RKPR) equation of state was utilized to address the density prediction error associated with the Peng-Robinson

(PR) equation of state, as mentioned in [52]. While the framework discussed in [20] has the capacity of simulating cavitating in-nozzle flows, no validation was performed for these conditions.

A key consideration in employing explicit density-based formulations utilising a real-fluid EoS for simulating multi-component, multi-phase scenarios is the non-linearity of the EoS. This non-linearity can lead to spurious pressure oscillations [49]. While quasi-conservative methodologies have been proposed as a possible solution, their applicability to cavitation conditions is yet to be validated, and they may introduce unphysical fuel heat-up due to energy conservation errors [52, 68]. However, in [20] effectively addressed this problem of spurious pressure oscillations by using a conservative methodology. The accuracy of the EoS is another relevant aspect in accurately simulating liquid-fuel injection systems. The PC-SAFT model has gained recognition for its superior performance over the cubic EoSs, a fact that has been well-established in the literature and confirmed in numerous studies [41,44,72]. The primary advantage of the PC-SAFT model, especially relevant to this context, lies in its capability to predict derivative properties. These include critical attributes such as compressibility and speed of sound, which play an important role in density-based explicit CFD formulations. Once the computation of residual entropy is performed, the transport properties of the mixture can then be determined using entropy scaling methodologies and multiphase mixture rules [66]. Central to this methodology are the Group Contribution (GC) methodologies [25] enabling the estimation of input parameters by considering the contributions from individual molecular groups. This predictive approach eliminates the need for expensive experimental measurements to calibrate thermophysical models, allowing for accurate estimates of the thermodynamic properties of new multi-component mixtures. In our previous publication [22], this approach was utilized to analyse the fuel properties of various substances, including oxymethylene dimethyl ethers (OME3-4) and alcohol blends with gasoline and diesel. Model results were benchmarked against experimental and computational data, observing good agreement with minor deviations. Finally, an additional complexity in such simulations arises from the simulation of the motion of the needle valve. Successfully simulating the needle movement in liquid-fuel injection systems is another crucial element in capturing cavitation phenomena and spray development [7,50,90]. The methodologies to incorporate needle movement in these simulations are diverse, ranging from entirely re-meshing the domain [31], adding and expanding cell layers [37] or interpolating between grids of different resolution but maintaining the same cell count [78]. However, these methods do not permit the needle to fully close and generally necessitate a minimum lift of about 2 %–8 % [60,102]. Cut-cell Immersed Boundary (IB) methods [60,61,102] present a potential solution to this challenge. A notable example can be found in [85], where the needle valve movement within a diesel injector was simulated demonstrating the efficacy of the IB method in handling complex cavitating turbulent flows.

In this work, we propose a numerical framework based on the foundations laid by the previous works [20,52]. These precursor studies employed a multiphase large-eddy Eulerian model, supplemented by the PR EoS/RKPR EOS, and VLE calculations. Our framework encompasses the intricate coupling of internal nozzle flow and spray development, as well as accounting for cavitation and needle movement. Key to these advancements is the integration of the PC-SAFT EOS, VT-flash algorithm [97], the IB Method [85], and entropy scaling techniques into the flow solver. Recognising the challenge associated with property measurement of new fuel blends, this framework retains a tuning-parameter-free approach. Implemented in the widely-used, open-source, CFD solver OpenFOAM, this sophisticated modelling methodology offers enhanced robustness, with its reliability validated against experimental data available for a single-component fuel. In particular, the implemented code is suited for injector flows operating in high pressure/temperature conditions and therefore validation is conducted for a benchmark case (Spray C) for which a large cross-validated database exists.

## 2. Numerical methodology

### 2.1. Governing equations and discretization

In the subsequent section, we outline the numerical methodology integrated into OpenFOAM where the thermodynamic closure is based on the PC-SAFT EoS. The methodology's validity is demonstrated through simulations of the Spray C037 [75] injector, performed under various operational conditions to mirror distinct experimental validation cases.

The three-dimensional Navier-Stokes equations for a multi-component, non-reacting mixture of  $n$  species were solved using the finite volume method.

- Continuity equation:

$$\frac{\partial \rho}{\partial t} + \nabla \cdot (\rho \mathbf{u}) = 0 \quad (1)$$

where  $\rho$  is the density,  $\mathbf{u}$  is the velocity vector, and  $t$  is the time.

- Species conservation equation:

$$\frac{\partial \rho Y_i}{\partial t} + \nabla \cdot (\rho Y_i \mathbf{u}) = 0 \quad (2)$$

where  $Y_i$  is the mass fraction of species  $i$ . In simulations of highly turbulent fuel injections using explicit solvers, the effect of species diffusion is negligible relative to convective mixing, justifying its exclusion [93].

- Momentum equation:

$$\frac{\partial (\rho \mathbf{u})}{\partial t} + \nabla \cdot (\rho \mathbf{u} \mathbf{u} + p \mathbf{I}) = \nabla \cdot \boldsymbol{\tau} \quad (3)$$

where  $\boldsymbol{\tau}$  is the viscous stress tensor,  $p$  is the pressure, and  $\mathbf{I}$  is the identity tensor. According to Stokes' hypothesis for a Newtonian fluid, the viscous stress tensor is given by:

$$\boldsymbol{\tau} = \mu \left( \nabla \mathbf{u} + (\nabla \mathbf{u})^T - \frac{2}{3} \nabla \cdot \mathbf{u} \right) \quad (4)$$

where  $\mu$  is the dynamic viscosity.

- Energy equation:

$$\frac{\partial E}{\partial t} + \nabla \cdot [(E+p)\mathbf{u}] = \nabla \cdot (\boldsymbol{\tau} \mathbf{u} - \mathbf{q}) \quad (5)$$

where  $E$  is the total energy and  $\mathbf{q}$  is the heat flux vector. Eq.(6) describes the heat flux vector as:

$$\mathbf{q} = -\lambda \nabla T \quad (6)$$

where  $\lambda$  is the thermal conductivity of the mixture.

To effectively handle the Navier-Stokes equations, a common approach is to employ operator splitting to separate the physical processes into hyperbolic and parabolic sub-steps that correspond to the left and right-hand sides of the equations, respectively. With respect to the hyperbolic sub-step, the multicomponent HLLC (Harten-Lax-van Leer-Contact) solver [91] is applied to solve the Riemann problem. The fluxes are calculated as:

$$\mathbf{F}^{HLLC} = \begin{cases} \mathbf{F}_L & \text{if } 0 \leq S_L, \\ \mathbf{F}_{*L} = \mathbf{F}_L + S_L(\mathbf{U}_{*L} - \mathbf{U}_L) & \text{if } S_L \leq 0 \leq S_*, \\ \mathbf{F}_{*R} = \mathbf{F}_R + S_R(\mathbf{U}_{*R} - \mathbf{U}_R) & \text{if } S_* \leq 0 \leq S_{*R}, \\ \mathbf{F}_R & \text{if } 0 \geq S_{*R}, \end{cases} \quad (7)$$

where  $\mathbf{U}_{*L,R}^*$  represents the star states [91],  $\mathbf{F}_{L,R}$  denote the left and right numerical fluxes, respectively, and  $S$  represents the wave speed. The formula utilized to calculate the speed in the middle wave, denoted as  $S_*$ , is given by:

$$S_* = \frac{p_R - p_L + \rho_L u_L (S_L - u_L) - \rho_R u_R (S_R - u_R)}{\rho_L (S_L - u_L) - \rho_R (S_R - u_R)} \quad (8)$$

The left and right wave speeds,  $S_L$  and  $S_R$  are calculated as:

$$\begin{aligned} S_L &= \min(u_L - c_L, u_R - c_R), \\ S_R &= \max(u_L + c_L, u_R + c_R) \end{aligned} \quad (9)$$

where  $u_R$  and  $u_L$  represent the velocity components in the right and left states, respectively. Furthermore,  $c_R$  and  $c_L$  correspond to the local speed of sound in the right and left states. This way of implementing the HLLC solver has been chosen as it shows good stability and it has been proved so in [67].

The MUSCL scheme, together with the van Albada limiter available in OpenFOAM was used to reconstruct the conservative variables at the cell faces. Pressure and speed of sound were calculated at cell centers and reconstructed at cell faces using the upwind scheme [65]; this is done to smoothen out the spurious pressure oscillations that might be generated due to the high non-linearity of the EoS (such as the PC-SAFT). The integration of the hyperbolic terms in time was performed using a third-order strong-stability-preserving Runge-Kutta method [84]:

$$\begin{aligned} \mathbf{U}^{(1)} &= \mathbf{U}^n + \Delta t \mathbf{H}(\mathbf{U}^n), \\ \mathbf{U}^{(2)} &= \frac{3}{4} \mathbf{U}^n + \frac{1}{4} [\mathbf{U}^{(1)} + \Delta t \mathbf{H}(\mathbf{U}^{(1)})] \\ \mathbf{U}^{(n+1)} &= \frac{1}{3} \mathbf{U}^n + \frac{2}{3} [\mathbf{U}^{(2)} + \Delta t \mathbf{H}(\mathbf{U}^{(2)})] \end{aligned} \quad (10)$$

where  $\mathbf{U}$  represents the vector of conservative variables, and  $\mathbf{H}$  corresponds to the numerical approximation of the flux function.

To solve the parabolic terms in the momentum equation, an implicit diffusion correction equation for velocity [23] was employed:

$$\frac{\partial (\rho \mathbf{u})}{\partial t} - \nabla \cdot (\mu \nabla \mathbf{u}) - \nabla \cdot (\mathbf{T}_{ext}) = 0 \quad (11)$$

The inter-component coupling present in the stress tensor ( $\mathbf{T}_{ext}$ ) is handled explicitly:

$$\mathbf{T}_{ext} = \mu \left( (\nabla \mathbf{u})^T - \frac{2}{3} \nabla \cdot \mathbf{u} \right) + \mathbf{f}_{ib} \quad (12)$$

where  $\mathbf{f}_{ib}$  represents the volumetric source term of the immersed boundary model.

The IB volumetric source term is determined by calculating the difference between the fluid velocity and the IB solid velocity, divided by the time step (as described in Eq.(13)). To localize the effect of the source term, it is multiplied by the IB mask, which distributes the impact to all cells within the IB region, rather than just at the interface. For a more comprehensive understanding of the implementation specifics, please refer to the details provided in [85].

$$\mathbf{f}_{ib} = \alpha_{ib} \frac{\mathbf{u}_{ib} - \mathbf{u}_{fluid}}{\Delta t}, \quad \alpha_{ib} \in [0, 1] \quad (13)$$

To discretize the time derivatives, a straightforward Euler implicit method was employed, first-order accurate in time. However, the

solution accuracy was ensured by utilizing the CFL (Courant-Friedrichs-Lewy) criterion for the hyperbolic operator to determine the global time step. The Green-Gauss theorem was applied to evaluate the divergences, gradients, and Laplacians in the parabolic terms. Linear interpolation was used to interpolate variables from cell centers to cell faces, enabling the calculation of Gaussian integrals in the parabolic terms. The parabolic terms in the energy equation are explicitly solved.

The Wall Adaptive Large Eddy (WALE) model, known for its favourable performance near walls [56], was utilized to provide the required turbulent closure for the turbulent viscosity:

$$\mu_t = \rho L_s^2 \frac{(S_{ij}^d S_{ij}^d)^{3/2}}{(S_{ij} S_{ij})^{5/4} + (S_{ij}^d S_{ij}^d)^{5/4}} \quad (14)$$

In this equation,  $S_{ij}$  represents the rate of strain tensor, while  $S_{ij}^d$  stands for the traceless symmetric portion of the squared strain in the velocity gradient tensor. The length scale,  $L_s$ , is determined based on the filter size and the distance from the cell to the wall,  $d_{wall}$ , and is expressed as:

$$L = \min\{kd_{wall}, C_w V^{1/3}\} \quad (15)$$

T model constants comprise the von Karman constant,  $k = 0.41$ , and  $C_w = 0.325$ .

To prevent the overall simulation time step from being limited by the smallest length scale in high aspect ratio cells, a modified Local Time Stepping (LTS) methodology has been implemented, inspired by previous work [16]. In this approach, each cell undergoes a local time step update according to:

$$\Delta t_{cell} = \min\left(\min_{face \in cell} \left(\frac{V_{cell}/A_{face}}{(c + \mathbf{u}_{face} \cdot \mathbf{n}_{face})d}\right), \Delta t_{sim}\right) \quad (16)$$

where  $V$  is the volume of the cell,  $A$  is the area of the face,  $\mathbf{u}_{face}$  is the velocity of the fluid,  $\mathbf{n}_{face}$  is the normal vector of the face,  $c$  is the speed of sound,  $d$  are the geometrical dimensions of the cell, and  $\Delta t_{sim}$  is the maximum time step specified at the initialization of the simulation

## 2.2. Thermodynamic closure

The thermodynamic closure is based on the PC-SAFT EoS, a derived theoretical model based on perturbation theory [24]. It separates the intermolecular potential energy of a fluid into repulsive and attractive interactions. To calculate the repulsive contribution, the model defines a reference fluid composed of spherical segments that form molecular chains. The attractive interactions, represented as perturbations to the reference system, are accounted for using a dispersion term [24]. Additionally, the model can include an association term [25] to consider intermolecular bonds formed between segments with association sites, such as proton donors and acceptors. An example of self-association is the formation of hydrogen bonds by the -OH group in alcohols [10]. The PC-SAFT is based on the Helmholtz free energy, which is derived as the sum of the contributions from the hard chain  $\tilde{a}_{hc}$ , dispersion  $\tilde{a}_{disp}$ , and association terms  $\tilde{a}_{assoc}$ :

$$\tilde{a}_{res} = \tilde{a}_{hc} + \tilde{a}_{disp} + \tilde{a}_{assoc} \quad (17)$$

The hard-chain term  $\tilde{a}_{hc}$  or a mixture of  $n_c$  components is given by:

$$\tilde{a}_{hc} = \bar{m} \tilde{a}_{hs} - \sum_i^{n_c} x_i (m_i - 1) \ln g_{ii}^{hs}(\sigma_{ii}) \quad (18)$$

$\bar{m}$  represents the mean segment number in the system,  $x_i$  is the mole fraction of component  $i$  in the fluid,  $\tilde{a}_{hs}$  is the hard sphere contribution,  $g_{ii}^{hs}$  is the average radial distribution function of the hard-sphere fluid, and  $m_i$  is the number of segments per chain for component  $i$ . The dispersion term  $\tilde{a}_{disp}$  is defined as:

$$\tilde{a}_{disp} = -2\pi\rho_m I_1(\eta, \bar{m}) \overline{m^2 \varepsilon \sigma^3} - \pi\rho_m \bar{m} C_1 I_2(\eta, \bar{m}) \overline{m^2 \varepsilon^2 \sigma^3} \quad (19)$$

$\rho_m$  is the molecular density. Details about the terms  $I_1(\eta, \bar{m})$ ,  $I_2(\eta, \bar{m})$ , and  $\overline{m^2 \varepsilon^2 \sigma^3}$  can be found in [24]. The association contribution to the Helmholtz free energy, as stated in [10,32,33], can be computed using the following expression:

$$\frac{\tilde{a}_{assoc}}{RT} = \sum_i X_i \left[ \sum_{A_i} \left[ \ln x^{A_i} - \frac{x^{A_i}}{2} \right] + \frac{M_i}{2} \right] \quad (20)$$

where  $M_i$  represents the number of association sites on each molecule of component  $i$ , and  $x^{A_i}$  is the mole fraction of molecules not bonded at site  $A$  for component  $i$ , which is given by:

$$x^{A_i} = \left[ 1 + \sum_j \sum_{B_j} \rho_j x^{B_j} \Delta^{A_i B_j} \right]^{-1} \quad (21)$$

where  $\sum_{B_j}$  represents summation over all sites on the molecules of component  $j$ :  $A_j, B_j, C_j$  etc. Also  $\rho_j = x_j \rho_{mixture}$  is the molar density and  $\Delta^{A_i B_j}$  the association strength.

The mixture parameters  $\sigma_{ij}$  and  $\varepsilon_{ij}$ , which are defined for every pair of unlike segments, are modeled using a Berthelot-Lorentz combining rule:

$$\sigma_{ij} = \frac{1}{2} (\sigma_i + \sigma_j) \quad (22)$$

$$\varepsilon_{ij} = \sqrt{\varepsilon_i \varepsilon_j} (1 - k_{ij}) \quad (23)$$

where  $k_{ij}$  is the binary interaction parameter. For more information on the derivation of the PC-SAFT EoS equations the reader is directed to the original publication of the model [24,25].

The input parameters required for conducting PC-SAFT computations include the number of chain segments ( $m$ ), the segment diameter ( $\sigma$ ), and the depth of pair potential divided by the Boltzmann constant ( $\varepsilon/k$ ). Each component must be individually defined with these parameters. Adjusted values based on empirical density and vapor pressure data can be found in the literature [24,25,92]. However, to be consistent with our previous work [22], this study is designed to introduce a more universal and predictive approach. Therefore, we employ a Group Contribution (GC) method to estimate these input parameters. In this study, we've implemented the Group Contribution (GC) method as proposed in [89]. This method, which has demonstrated satisfactory results in previous applications, dissects the molecular structure into simpler first-order groups and more complex second-order groups. The PC-SAFT parameters ( $m$ ,  $\sigma$  and  $\varepsilon/k$ ) are then calculated by accounting for the individual contributions from each group ( $m_i$ ,  $\sigma_i$  and  $\varepsilon_i/k_i$ ), as demonstrated in the following mathematical expressions:

$$m = \sum_i^{n \text{ groups}} (n_i m_i)_{FOG} + \sum_i^{n \text{ groups}} (n_i m_i)_{SOG} \quad (24)$$

$$m \sigma^3 = \sum_i^{n \text{ groups}} (n_i m_i \sigma_i^3)_{FOG} + \sum_i^{n \text{ groups}} (n_i m_i \sigma_i^3)_{SOG} \quad (25)$$

$$m \varepsilon / k = \sum_i^{n \text{ groups}} (n_i m_i \varepsilon_i / k_i)_{FOG} + \sum_i^{n \text{ groups}} (n_i m_i \varepsilon_i / k_i)_{SOG} \quad (26)$$

When dealing with associating components, identifying the type of bonding is necessary. In their study focusing on alkanols, Huang et al. [32] recommend the use of both 3B and 2B bonding models. However, due to the absence of a persuasive case for using the more intricate 3B model, this study opts for the less complex 2B approach. Additionally, the 2B model has been successfully utilized by Gross et al. [25] to characterize compounds like ethanol, methanol, and pentanol, among others. Two more parameters pertaining to pure components, namely

the effective association volume ( $k^{AB}$ ) and the association energy ( $\epsilon^{AB}/k$ ), are employed for associated components. These parameters can also be calculated utilizing the GC method proposed in [89]. Lastly, the Quantitative Structure Property Relationship (QSPR) method introduced in [86] was applied to estimate the binary interaction parameter ( $k_{ij}$ ).

$$k_{ij}^{QSPR} = \sum_{L=1}^{N_d} c_L D_L(\bar{p}_i, \bar{p}_j) \quad (27)$$

where  $N_d$  represents the number of descriptors, and  $D_L(\bar{p}_i, \bar{p}_j)$  are the descriptors with corresponding regression coefficients  $c_L$ .

As pointed out in [24], the PC-SAFT EoS is applicable to mixtures of small spherical molecules such as gases, nonspherical solvents, and chainlike polymers. Moreover, when applied to vapor–liquid equilibria of mixtures, the equation of state shows substantial predictive capabilities and good precision for correlating mixtures. Finally, they mention that the applicability of the proposed model to polymer systems was demonstrated for high-pressure liquid–liquid equilibria of a polyethylene mixture. The pure-component parameters of polyethylene were obtained by extrapolating pure-component parameters of the n-alkane series to high molecular weights.

### 2.3. Vapour Liquid equilibrium (VLE) calculations

The methodology detailed and validated in [22,96] is optimized via parallelization utilizing the OpenMP library. In particular, parallelisation is needed to construct the thermodynamic table that will then be used by numerical solver. With the use of OpenMP, the table formulation requires 2 days instead of weeks for serial calculations. The algorithm featured in [96], and used in [22], leverages the PC-SAFT EoS to evaluate the stability of a homogeneous mixture, given a particular composition, density, and temperature. In situations where instability is detected, the algorithm determines the vaporized portion of the substance and the compositions of both phases, as well as the resultant equilibrium pressure through a TV-flash calculation. TV-flash can be seen as an algorithm where volume and temperature are used as independent variables for minimising the Helmholtz free energy rather than the Gibbs free energy (as in the PT-Flash algorithm) for the multiphase problem [96]. A homogeneous mixture at a given temperature  $T$  is considered stable if the tangent plane, drawn at the composition  $z$  and density  $\rho$  on the Helmholtz free energy surface, does not intersect this energy surface at any other location. To verify stability, the homogeneous mixture is intentionally partitioned into two phases, with one phase existing in a nominal or minute amount, referred to as the trial phase. If there is no reduction in the Helmholtz free energy for any potential two-phase combinations, then the mixture is recognized as stable. The tangent plane distance (TPD) function employed is defined as follows:

$$TPD = \frac{P' - P^*}{RT} + \sum_{i=1}^{nc} \rho' x_i' (\log f_i' - f_i^*) \quad (28)$$

The variables represented with primes correspond to values calculated under trial conditions, while those with an asterisk indicate values calculated under feed conditions.  $R$  stands for the universal gas constant, and  $f_i$  refers to the fugacity of component  $i$ . The initialization of the iterative minimization process incorporates Raoult's law and Wilson's correlation [99], along with Michelsen's [80] and Mikyska and Firoozabadi's [53] work. This combination allows the derivation of an expression for the initial composition of the liquid phase (represented as  $l_i$ ) and the vapor phase (represented as  $v_i$ ). Here,  $z_i$  denotes the total initial composition.

$$v_i = \frac{z_i P_{ini}}{P_i^{sat}} = \frac{z_i}{P_i^{sat} \left( \sum_{i=1}^{nc} \frac{z_i}{P_i^{sat}} \right)} \quad \text{and} \quad l_i = \frac{z_i P_i^{sat}}{P_{ini}} = \frac{z_i P_i^{sat}}{\sum_{i=1}^{nc} z_i P_i^{sat}} \quad (29)$$

If a two-phase regime is identified during the stability analysis, the algorithm continues by performing TV-flash calculations, where the objective is to minimize the Helmholtz energy for a given density, temperature, and composition. In both stability analysis and flash calculations, Newton's method is employed to solve the optimization problem. To determine the step length in the Newton method, an inexact line search is conducted. This search aims to find a step length that satisfies the Wolfe conditions [58]. Eq.(30) needs to be solved to calculate the direction ( $p_k$ ) followed in the search for the optimal solution.

$$\nabla^2 f_k p_k = -\nabla f_k \quad (30)$$

The equation involves the Hessian ( $\nabla^2 f_k p_k$ ) and the gradient ( $\nabla f_k$ ) of the objective function. To guarantee the positive definiteness of the Hessian matrix, we employ a modified Cholesky factorization algorithm [79]. For a more detailed explanation of the methodology, please refer to [96].

The thermodynamic closure has been validated thoroughly for various types of multi-component fuel mixtures as demonstrated in a previous study of the authors' group [28]. The present investigation incorporates it successfully in the frame of a density-based flow solver.

### 2.4. Calculation of thermal conductivity

Following up from the accurate results produced in our prior study for hydrocarbon mixtures [38], we are employing the same residual entropy scaling method [30] for the calculation of thermal conductivity in the present investigation [50]. Within this approach, the thermal conductivity is normalized via a benchmark value, represented as  $\lambda^{ref}$ , which is uniquely tailored for each component as detailed below:

$$\lambda_i^{ref} = \lambda_{CE,i}^{ref} + a(s^*) \lambda_i^{correct} \quad (31)$$

In the above equation,  $\lambda_{CE}^{ref}$  represents the Chapman-Enskog formula for thermal conductivity, which is mainly applicable to monoatomic gases. The element  $\lambda_i^{correct}$  serves as an adjustment parameter for polyatomic fluids. Additionally,  $a(s^*)$  is defined as a transitional function, detailed as follows:

$$a(s^*) = \exp\left(\frac{-s^{res}}{\sum_{i=1}^{nc} x_i s_{c,i}^{res}}\right) \quad (32)$$

In this context,  $x_i$  denotes the mole fraction of the  $i$  component in a mixture comprising  $nc$  components. The term  $s^{res}$  represents the residual entropy, and  $s_{c,i}^{res}$  signifies the residual entropy value of component  $i$  at its critical point.

$$s^{res} = -T \frac{\partial a^{res}}{\partial T} - \tilde{a}^{res} \quad (33)$$

Following this, the dimensionless thermal conductivity, represented by  $\lambda^*$ , is computed as a function of the normalized residual entropy, denoted as  $s^*$ , in the following way:

$$\ln(\lambda^*) = \ln\left(\frac{\lambda}{\lambda^{ref}}\right) = A_{mix}^{\lambda} + B_{mix}^{\lambda} s^* + C_{mix}^{\lambda} (1 - \exp(s^*)) + D_{mix}^{\lambda} s^{*2} \quad (34)$$

In this equation, the reduced residual entropy is calculated using the mean segment number, represented by  $\bar{m}$ , which is the sum of the products of the mole fraction  $x_i$  and segment number  $m_i$  for each of the  $nc$  components.

$$s^* = \frac{s^{res}}{\bar{m}} \quad (35)$$

Initially, the entropy scaling method was employed exclusively for individual components. Hence, in this research, mirroring the approach in [38], an empirical mixing rule has been applied to both the coefficients and the reference thermal conductivity, as follows:

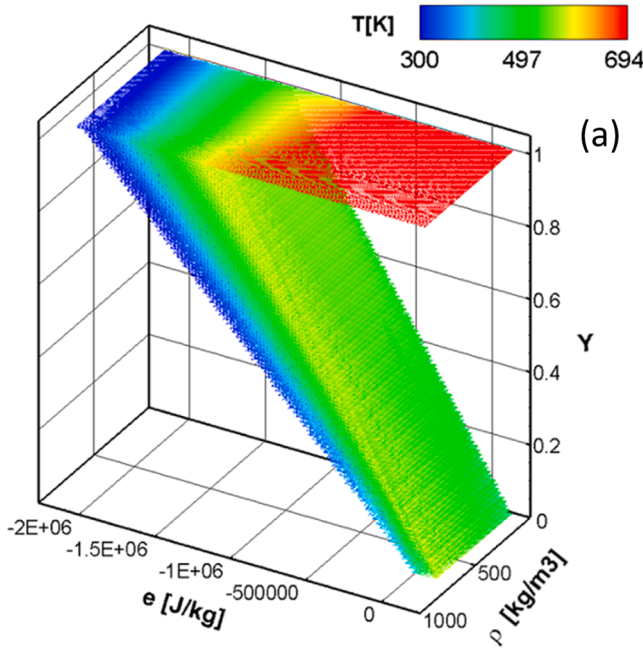


Fig. 1. Example of three-dimensional table used to calculate the thermophysical properties of air-fuel mixtures indexed by the mass fraction of fuel, density, and internal energy of the mixture (n-dodecane and nitrogen).

$$X_{mix} = \frac{\sum_i^{nc} x_i m_i \sigma_i^2 X_i}{\sum_i^{nc} x_i m_i \sigma_i^2} \quad (36)$$

In this equation, X can represent any one of the coefficients  $[A^i, B^i, C^i, D^i]$  or  $\lambda_{ref}$ . If the mixture conditions lie within the VLE regime, the mixing rule simply becomes a weighted average operation, utilizing the vapor volume fraction, denoted by  $\alpha$ , along with the thermal conductivities for the liquid and gas phases, expressed as  $\lambda_l$  and  $\lambda_g$  respectively.

$$\lambda_{VLE} = \alpha_g \lambda_g + (1 - \alpha_g) \lambda_l \quad (37)$$

### 2.5. Calculation of viscosity

Lötgering-Lin and Gross [48] applied the entropy scaling model for computing dynamic viscosity as well [70]. For a singular component, the reduced dynamic viscosity, symbolized by  $\mu_i^*$ , can be calculated using the following formula:

$$\ln(\mu_i^*) = A_i^* + B_i^* s^* + C_i^* s^{*2} + C_{mix}^* s^{*3} \quad (38)$$

The methodology for determining the value of the mixture is detailed in reference [98]. If the mixture is in a VLE state, the mixing rule provided by Beattie and Whalley [8] is utilized.

$$\mu_{VLE} = \alpha_g \mu_g + (1 - \alpha_g) \left( 1 + \frac{5}{2\alpha_g} \right) \mu_l \quad (39)$$

### 2.6. Tables structure

In the context of highly turbulent multi-component simulations, when using explicit density-based diffuse interface solvers, the impact of species diffusion terms in the energy and continuity equations is often considered negligible. This assumption arises primarily because of the robust convective mixing that characterizes these simulations, which significantly overshadows any diffusion effects. This model simplification enables the utilization of just two continuity equations: one to monitor the multicomponent fuel mixture and the other to track the mixture of fuel and ambient gas. By using these two equations, it's possible to consolidate all essential information regarding the properties

Table 1

Benchmark cases relevant to injector flows employed for the validation of the numerical methodology implemented in the current study.

Benchmark case	Numerical predictions or Experimental data
Case A - Spray C in-nozzle flow	X-ray phase-contrast radiographies [88]
Case B - Spray C in-nozzle flow	CONVERGE simulations [26]
Case C - Spray C Near-Nozzle Spray	x-ray radiography measurements [81]
Region	
Case D - Spray C cone angle	ECN data [76]

of the working fluids into a three-dimensional table, organized by fuel mass fraction, density, and internal energy. Table points are evenly distributed on a linear scale (1000 points for density and internal energy and 100 points for fuel mass fraction), with trilinear interpolation used to calculate the thermodynamic and transport properties of the multiphase, multicomponent mixture (among which temperature, specific heat, pressure, viscosity, and vapour fraction) in each cell of the domain, as illustrated in Fig. 1.

The development of this 3D table poses a challenge in terms of including in the table only the thermodynamic states of the mixture that are both physically meaningful and relevant. To address this, realistic minimum and maximum values for density and internal energy values for each fuel mass fraction are determined and used to compute the table, taking into account the specific scenarios where the table will be applied. Such limits have been set to ensure that the table is suitable for any condition expected in the relevant simulation and exceed to a certain extent of safety the CFD-predicted density and internal energy values. In fact, if table bounds are reached during solution, the simulation becomes unstable. More details on how the table is computed can be found in our previous work [22]. Finally, as pointed out in [39], constructing the thermodynamic table prior to the simulations result in a much more efficient than the on-the-fly calculation of the Helmholtz EoS, by almost one order of magnitude of the computational time.

## 3. Results

In this section, we present the results obtained from different validation test cases. A is intended to assess the efficacy of our CFD code by comparing it against the experimental findings derived for the in-nozzle flow of the ECN Spray C injector [88]. Case B aims to benchmark the accuracy of the code against widely-employed commercial software, emphasising on the modelling of in-nozzle cavitating flows [26]. Case C is set up to examine the accuracy of the proposed numerical framework in illustrating the effect of nozzle geometry on the near-nozzle spray cone angle of the ECN Spray C injector [75,88]. Finally, Case D was devised as a comparative study focusing on the cone angle of the ECN Spray C. Table 1 summarises the test cases performed against experimental results to validate the numerical approach proposed in the current study, along with the numerical/thermodynamic approaches against which our methodology has been compared to in each case, as well as the source of available experimental data as already presented in previous work of the group. Further verification studies in simpler benchmark cases including a 1D shock tube and a Reyleigh-collapse case have been conducted and presented in [9].

### 3.1. Geometry and numerical grids

The developed numerical framework validated using the Spray C037 injector nozzle, a well-studied component within the Engine Combustion Network (ECN). It is worth noting that the precise geometry of this nozzle has been accurately measured as part of the ECN's extensive research initiatives. For a comprehensive understanding of the Spray C037 injector nozzle geometry, readers can refer to the resources available on the official ECN website [76]. The computational domain, as depicted in Fig. 3, comprises a rectangular area linked to the fuel

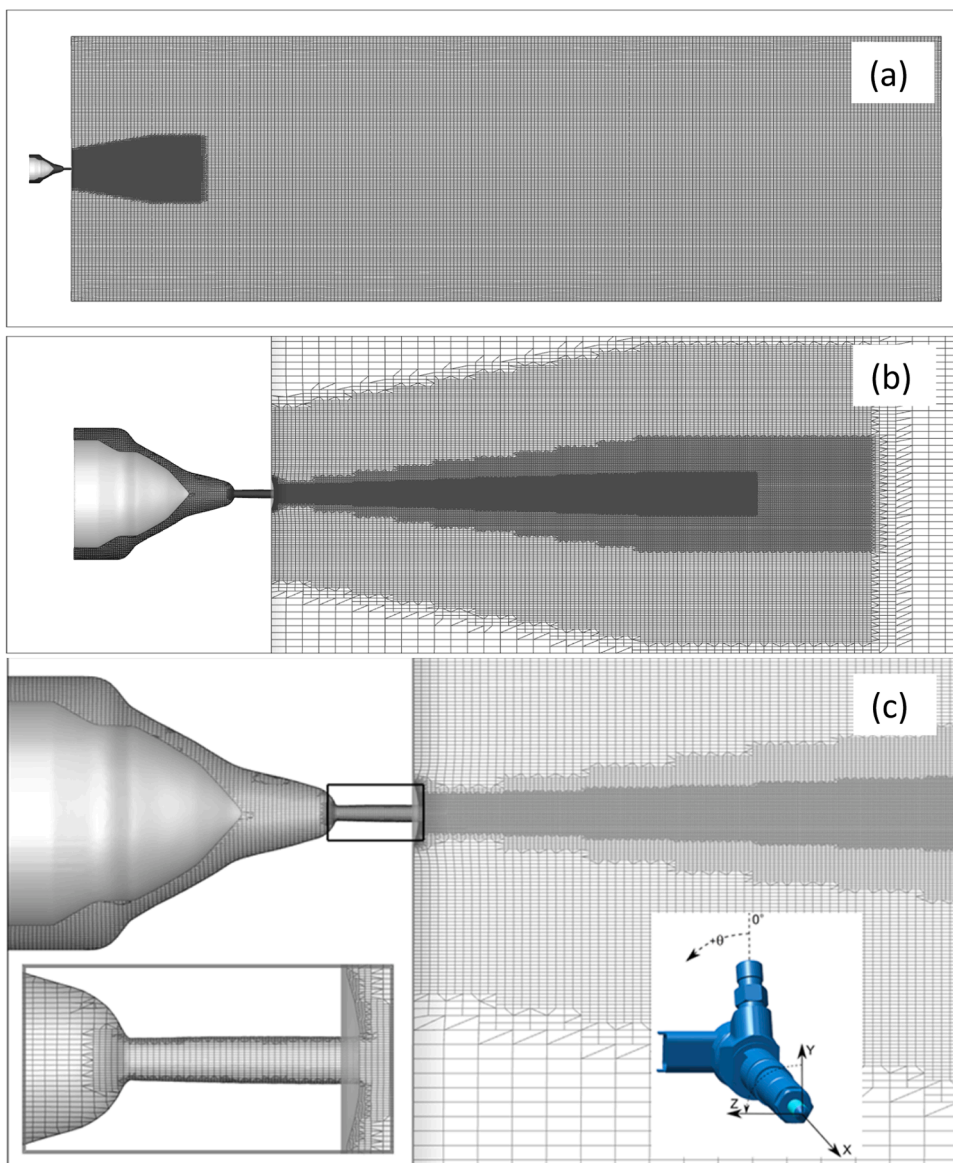


Fig. 2. Numerical grid for the Spray C037 injector nozzle: (a) overall domain, (b) detailed view of the near-nozzle region, and (c) close-up of the in-nozzle region, and ECN coordinate system for the Spray C and Spray D injectors [82].

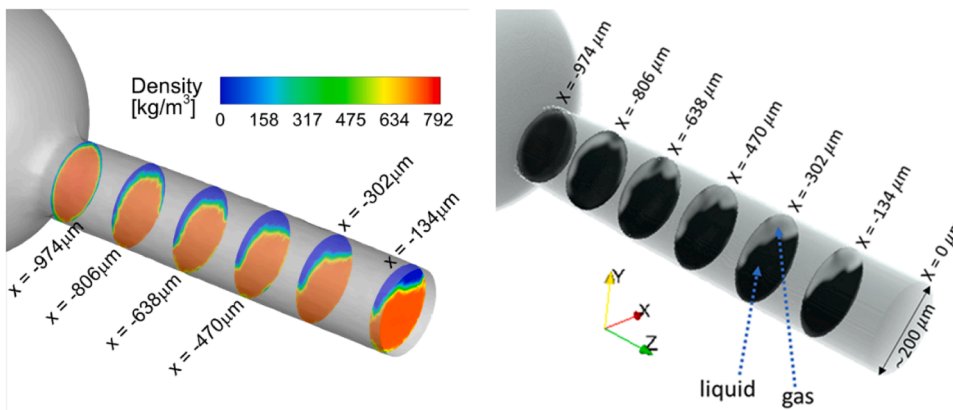


Fig. 3. This figure contrasts our ECN Spray C in-nozzle flow simulation results (left) with experimental results from [39] (right). The experimental image, a slice of the fully reconstructed CT volume, reveals flow separation and cavitation nearing the nozzle exit (nozzle length  $\sim 1$  mm). The coordinate system has  $x = 0 \mu\text{m}$  at the nozzle tip. High and low intensities represent liquid and gas phases, respectively.

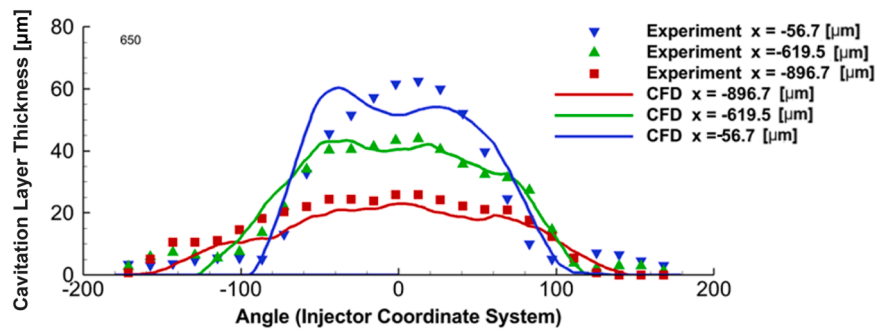


Fig. 4. Instantaneous gas layer thickness distributions at three cross-sections plotted as a function of angular position for injection Case A. The experimental results presented in [88] are compared with the current numerical simulations.

injector, with overall dimensions of  $32 \times 105$  mm. To streamline the process of mesh generation, we employed an adaptive mesh refinement technique. We followed a cartesian blocking strategy, incorporated with a static local coarsening/refinement approach, and adjusted the grid resolution along the spray break-up trajectory to enhance computational efficiency. In the core of the orifice, the resolution is approximately  $10 \mu\text{m}$ , with refinement closer to the walls, reaching down to a minimum cell size of around  $2 \mu\text{m}$ . This resolution is in agreement with the Taylor length scales, represented by the equation  $\lambda_g = \sqrt{10Re^{0.5}D}$ , where  $D$  is an indicative length of the geometry; in this case, the nozzle hole exit diameter. The flow near the wall was addressed using two specific wall functions: (i) the  $kqRWallFunction$  [47] for managing the turbulent kinetic energy, and (ii) the  $nutkwallfunction$  [47] for handling the turbulent viscosity, as realised in the OpenFoam framework. Finally, walls were considered adiabatic, thus ZeroGradient boundary conditions were imposed for temperature at each boundary.

### 3.2. Case A: validation of ECN spray C in-nozzle flow simulation against experimental data

This section explores ECN Spray C in-nozzle flow simulation, juxtaposing it with the findings documented in [88]. In this referenced work, an x-ray-based 3D visualization of the ECN Spray C internal flow was achieved with an impressive  $2 \mu\text{m}$  pixel resolution. The simulation, conducted at a constant maximum lift [78], replicates the injection conditions with a fuel pressure of 150 MPa, an ambient pressure of 0.1 MPa and a constant temperature of  $25^\circ\text{C}$  for both the fuel and the ambient environment. The accuracy of the simulations is assessed by examining the vapor phase distribution within the orifice.

Fig. 3 offers a qualitative comparison between our simulation and the experimental results drawn from [88], since quantitative information cannot be extracted by x-ray phase contrast imaging. These results are portrayed as slices from the fully reconstructed computed-tomography volume, capturing the flow separation and cavitation cloud approaching throughout the orifice length until its exit. According to the coordinate system in use, the nozzle tip is defined at  $x = 0 \mu\text{m}$ . Areas of high and low intensity correspond to the liquid and gas phases. The comparison of the two images reveals a high degree of similarity between the simulated and actual vaporous structures.

Fig. 4 builds upon this analysis by offering a quantitative comparison of the gas layer thickness at three specific cross-sections, defined in relation to angular position. Within this reference framework, the origin is centrally positioned at the orifice exit, and all positions within the orifice are described by negative "x" coordinates. In alignment with the method described in [26], a particular gas volume fraction threshold of 0.15 was selected to ensure precise agreement between the simulation and experimental results at the  $-896.7 \mu\text{m}$  location. This specific threshold provided an accurate representation of the gas layer extent and orientation at the other two cross-sections, namely  $-619.5 \mu\text{m}$  and  $-56.70 \mu\text{m}$ , albeit with a minor reduction in thickness, which should be

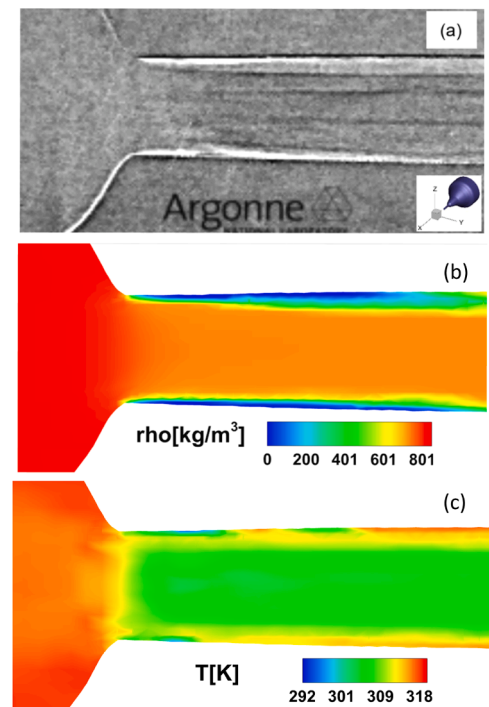


Fig. 5. (a) Experimental results [26], showing the phase contrast corresponding to cavitation inside the Spray C injector; simulation results of (b) the density distribution inside the injector, highlighting the vapour formation on the wall and (c) the temperature distribution inside the injector, highlighting the effects of viscous heating, depressurization-induced liquid cooling, and cavitation.

considered to be within the experimental uncertainty of x-ray-based visualisation [35]. Even with these slight variations, the overarching trend remained consistent with the experimental findings.

Fig. 5 reveals the complex temperature distribution within the injector, offering insights into the contrasting effects of viscous heating and depressurization-induced liquid cooling. Notably, the figure emphasizes the substantial shear experienced along the orifice walls, resulting in heating due to viscous forces, with localized near-wall temperatures reaching around 313 K. Conversely, it's essential to point out that within portions of the nozzle orifice in the vicinity of the walls, where intense cavitation is evident, the temperature drops to around 295 K.

Moreover, the figure portrays the isentropic expansion of the liquid, leading to cooling as the liquid expands from the inlet pressure and sac temperature to the orifice exit pressure. This cooling process culminates in a temperature decline to approximately 304 K, aligning with the minimum value detected at the orifice exit. Together, these observations reveal that both viscous heating and depressurization-induced cooling

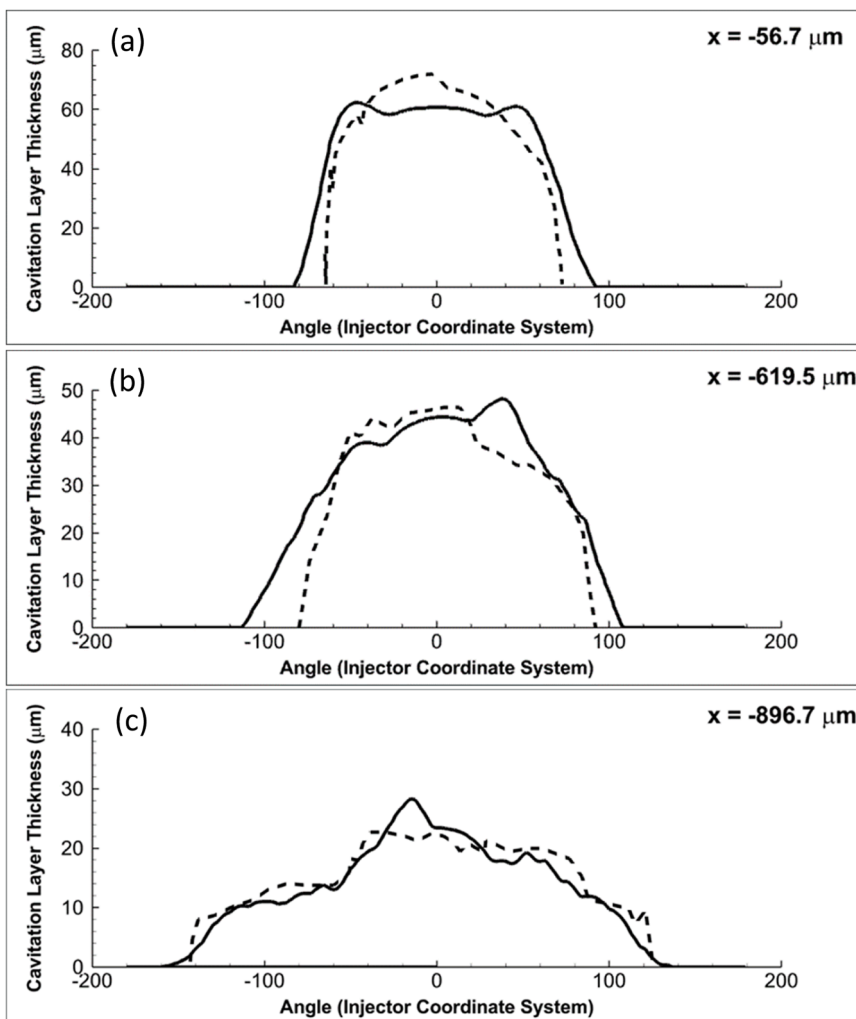


Fig. 6. Gas layer thickness plotted as a function of angular position for injection Case B (a)  $x = -56.7 \mu\text{m}$ , (b)  $x = -619.5 \mu\text{m}$  and (c)  $x = -896.7 \mu\text{m}$ . Current CFD predictions (continuous line) compared those presented in [26].

play significant roles in shaping the temperature distribution within the injector. Unlike the barotropic models typically used for in-nozzle simulations, which don't provide temperature distributions, the methodology presented here can capture these intricate temperature dynamics. This ability to model temperature variations is a significant advantage, revealing that both viscous heating and depressurization-induced cooling play crucial roles in shaping the temperature distribution within the injector.

### 3.3. Case B: comparative study of the ECN spray C in-Nozzle flow simulation results with existing software

In this section, we replicate the analysis carried out in the previous section (i.e. Spray C nozzle), yet at different operating conditions. We focus on the gas layer thickness at three specific cross-sections, as shown in Fig. 6. Results of the present investigation have been produced by employing purely physics-informed thermodynamic and phase-change modelling approaches. The baseline study in [26] was performed using the commercial CFD software CONVERGE v2.4. A large eddy simulation (LES) framework with the one-equation dynamic structure model was used to model the effect of turbulence on the flow field. The phase change due to cavitation was modeled via the homogeneous relaxation model (HRM), which assumes a first-order relaxation of vapor quality towards the equilibrium value. The gas phases were described by the Redlick-Kwong equation of state (EOS), while the liquid was

modeled as compressible using an exponential barotropic fluid assumption. Spatial and temporal discretization was achieved with second-order and first-order respectively. A variable timestep algorithm was employed with a maximum CFL number of 0.4. The parameters for our simulation include n-dodecane as the fuel, an injection pressure of 150 MPa, an ambient pressure of 2.0 MPa, and a fuel temperature of 323 K. Based on the needle profile described in [26], we maintained a constant needle lift corresponding to its position 0.2 ms after SOI. The mass fraction of non-condensable N2 gas was set to 2E-5.

Our findings show good agreement with those available in the literature [26]. This comparison becomes particularly relevant, as unlike the established commercial software where calibration parameters such as liquid saturation density, viscosity, surface tension, or vapor pressure are commonly adjusted, our study takes a different, tuning-free approach. We consider all thermophysical parameters as functions of internal energy, density, and composition, allowing them to vary throughout the simulations. This approach provides a more detailed insight into the behaviour of the fluid dynamics within the injector, capturing localized temperature changes and allows the incorporation of novel synthetic fuels or complex fuel mixtures, as demonstrated by the authors in [22].

This approach could be particularly beneficial where experimental data might be limited or unavailable. Indeed, the main limitation when using cubic EOSs stems from the fact that the specified density of the vapour-liquid mixture used by the flow solver falls between the liquid

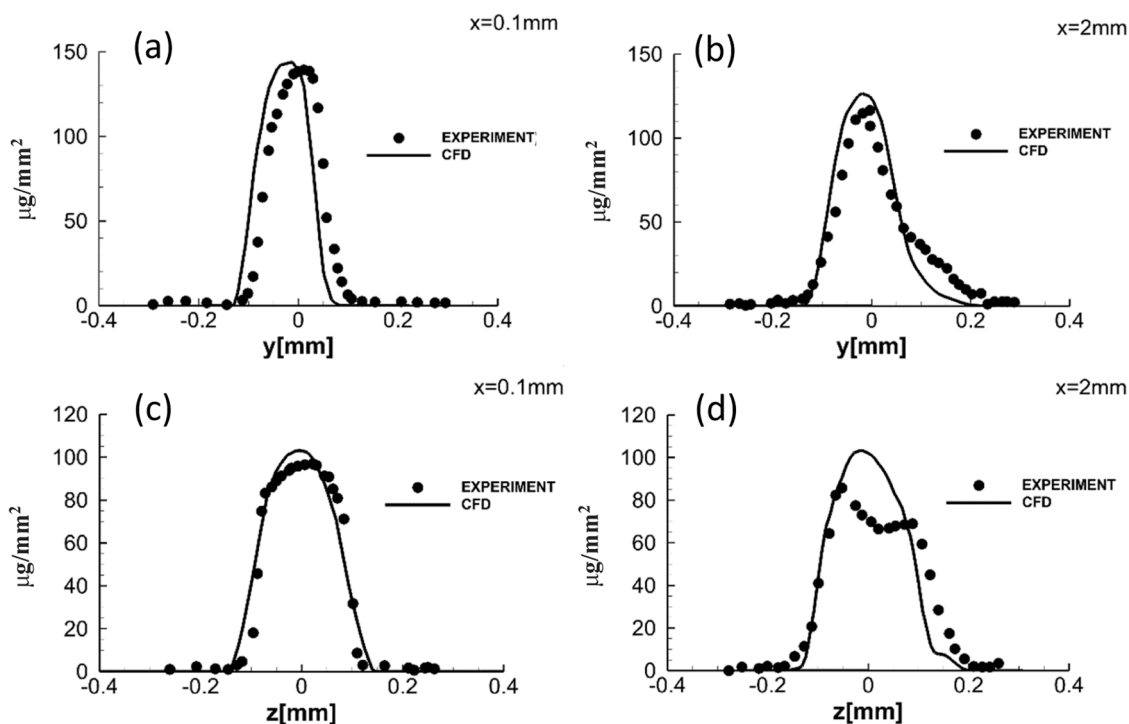


Fig. 7. Comparison between steady-state projected density profiles of fuel spray obtained from experimental measurements and numerical simulations for Spray C: (a) z-view,  $x = 0.1$  mm, (b) z-view  $x = 2$  mm, (c) y-view,  $x = 0.1$  mm, (d) y-view  $x = 2$  mm.

and vapor saturated densities in the PT diagram of the fuel, resulting in the target density being unavailable. On the other hand, the methodology proposed by the authors allows to calculate the target density since it implements the VT Flash algorithm as described in the manuscript.

### 3.4. Case C: validation in the spray C near-nozzle spray region

The specific simulation was performed to investigate whether the spray characteristics in the near-nozzle region were influenced by the in-nozzle two-phase flow topology. The same operating conditions used for x-ray radiography measurements of ECN Spray C were replicated, as described in [82]. Operating conditions included n-dodecane fuel, 150 MPa injection pressure, 2 MPa ambient pressure, and a uniform temperature of 25 °C for both fuel and surroundings. Previously obtained quantitative measurements using the monochromatic beam of the Advanced Photon Source of Argonne National Laboratory were used to validate the simulation.

Fig. 7 illustrates the projected density profiles of the fuel jet at  $x = 1$  mm and  $x = 2$  mm for Spray C from two orthogonal views. The focus on this near-nozzle region was intentional, as it allows a detailed examination of how the complex processes occurring within the nozzle, i.e., cavitation evolution, are reflected in the spray pattern just outside the nozzle. The decision to exclude additional density profiles beyond 2 mm is influenced by the divergence between the simulation classical vaporization initial conditions and the diffuse interface, VLE assumption, more relevant in high-pressure and high-temperature environments [12]. The figures reveal the asymmetric nature of the fuel distribution, a direct result of cavitation within the Spray C nozzle. The vapor cloud obstructing a portion of the hole exit area leads to a unimodal spray profile skewed in the -Y direction, showcasing the profound impact of the nozzle internal conditions on the emerging spray pattern. The discrepancies shown in Fig. 7, can be attributed to by emphasizing that the experimental data of Fig. 7 have been produced through x-ray radiography, a very delicate imaging technique. To name a few, uncertainty in the calculation of the absorption coefficient

(usually calculated in a precursor calibration study) or variation in the beam energy leading to beam hardening effects can lead to increased uncertainty of the experimental results [34]. Unavoidable uncertainty in the injector geometry and needle motion, e.g., wobble, can also add to the discrepancy between experiment and simulation. It has to be noted that experimental data were not associated with uncertainty in the original publication.

### 3.5. Case D: simulation of experimental cone angle in ECN spray C

In Case D, we focused on simulating the experimental cone angle for the ECN Spray C, as documented by the ECN [76]. This was the most computationally expensive simulation that has been performed in this study. It was performed using a grid of around 100 million cells and it was executed for approximately 3 weeks utilising 196 processors. Indeed, the selected time-step was of the order of  $10^{-9}$  s due to the spatial/temporal length scales that appear in the in-nozzle flow. This allowed to properly capture the coupling of in-nozzle flow and spray propagation. Finally, being an explicit solver, the parallelization works well, thus the use of 196 processors.

The cone angle is a critical variable in understanding how liquid fuel distributes as it ejects from the injector nozzle and is affected by factors such as the internal flow dynamics and cavitation within the injector. The simulation initial conditions were set considering an ambient temperature of 440 K, 363 K fuel temperature, and an injection pressure of 150 MPa. We utilized a computational grid containing 27 million cells, more extensive than in previous cases, to enable detailed refinements in the spray-chamber region. The simulation time selected for this study was 0.5 milliseconds. Fig. 8a reveals that the simulation is accurately capturing the correct cone angle for the ECN Spray C. The cone angle was measured by detecting the pixel brightness gradients of high-speed visualisation images highlighting locally the spray periphery [6]. Furthermore, to better visualize the cone angle in Fig. 8a, cells in a single-phase state, whether entirely liquid or gas, are assigned a vapor volume fraction value of 0.

Fig. 8b illustrates the mass fraction within the jet. The image

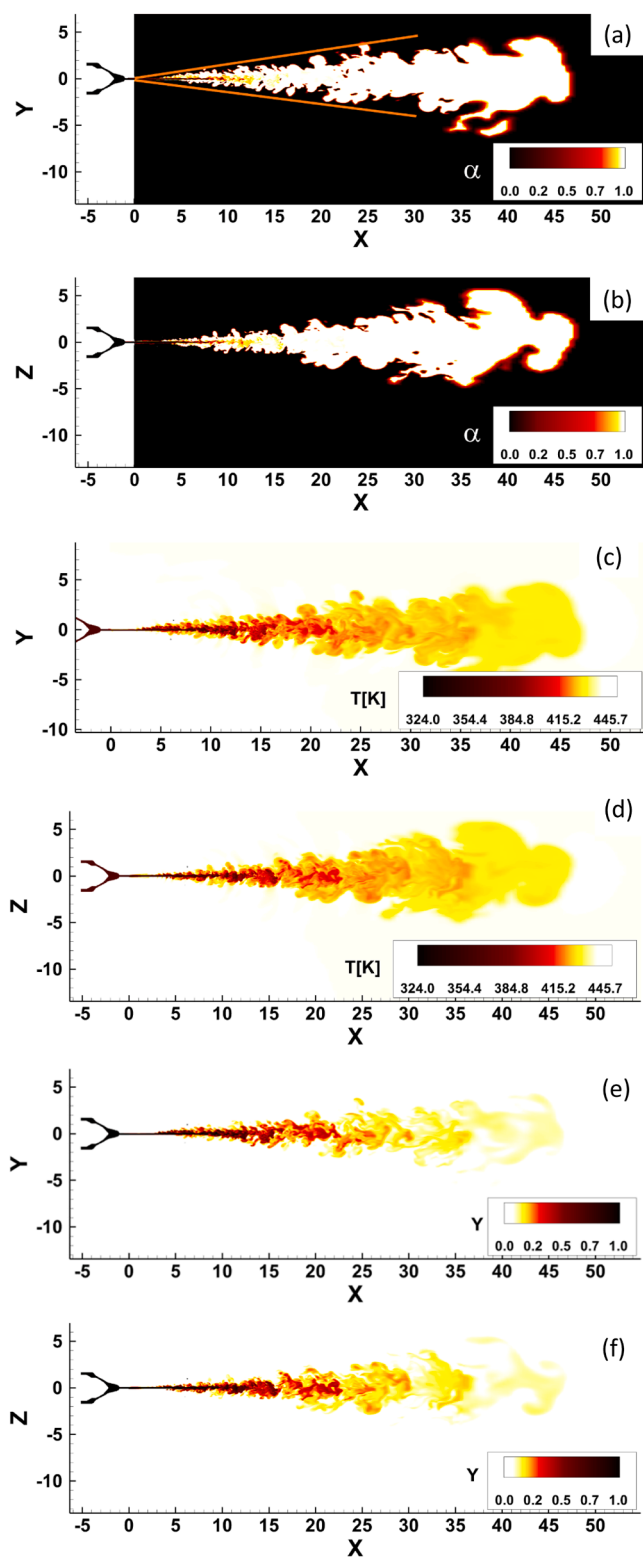


**Fig. 8.** Visualization of spray evolution during the steady injection phase (fixed needle) for Case D, featuring y-view (X-Z axis) and z-view (X-Y axis) as detailed in the ECN coordinate system for Spray C and D injectors (refer to Fig. 2). ECN measurements on plume growth, experimentally obtained up to 8 mm and subsequently linearly extended, are depicted with orange lines in image (a), corresponding to the z-view. Images (a-b) show the vapor volume fraction distribution and experimental cone angle, annotated in orange, measured by detecting pixel brightness gradients in high-speed visualization images that highlight the spray periphery. Images (c-d) illustrate the temperature distribution in the spray region, and images (e-f) detail the fuel mass fraction.

effectively captures the multiphase mixing process, revealing a formation that mirrors what is typically observed in experimental studies. Furthermore, Fig. 8c presents the temperature contours for both the in-nozzle and spray areas, clearly showing the rise in fuel temperature as it mixes with the warmer ambient gas within the combustion chamber. Notably, the areas of elevated temperature align closely with zones of pronounced shear-flow instabilities, predominantly of the Kelvin-Helmholtz type, which serve as the initial stages of jet disintegration as shown in Figs. 8e and 8f.

#### 4. Conclusions

A comprehensive flow solver with real-fluid thermodynamics was developed to simulate multi-component fluid mixtures, focusing on cavitating in-nozzle flow and sprays. The present investigation comes as a follow up to the previous study of the authors' group [22] where a thorough validation of the thermodynamic framework has been validated for different types of diesel, gasoline and aviation fuels. The main aspect of novelty of the presented work is the implementation of a robust and time effective flow solver based on the highly accurate PC-SAFT equation of state employed for thermodynamic closure. The capability of the present methodology to concurrently predict in-nozzle flow and spray atomisation at sub- and supercritical pressure/temperature conditions, advances the current state of the art with respect to numerical tools for highly-compressible injector flows. Its effectiveness was confirmed through detailed comparisons with experimental data, evaluating its precision in predicting flow characteristics such as the gas layer thickness, projected density profiles for the spray region in close proximity to the nozzle, and the cone angle of the fuel injection process. By leveraging the PC-SAFT, VLE computations, entropy scaling methodologies, and GC methodologies, the model not only accounts for thermal effects and local variations of the thermophysical properties but also considers the influence of real-fluid behaviour in capturing phenomena such as cavitation, atomization, and vaporization under high-pressure/high-temperature conditions. The model adaptability, lack of dependence on adjustable parameters, and consistency with precise experimental outcomes further affirm its dependability and effectiveness in accurately representing complex spray dynamics.

#### CRedit authorship contribution statement

**R. Bellini:** Writing – review & editing, Writing – original draft, Visualization, Validation, Software, Methodology, Investigation, Formal analysis, Data curation, Conceptualization. **C. Rodriguez:** Writing – review & editing, Writing – original draft, Visualization, Validation, Supervision, Software, Methodology, Investigation, Formal analysis, Data curation, Conceptualization. **I.K. Karathanassis:** Writing – review & editing, Supervision, Resources, Project administration, Funding acquisition, Conceptualization. **L. Pickett:** Writing – review & editing, Validation, Supervision, Data curation, Conceptualization. **M. Gavaises:** Writing – review & editing, Supervision, Resources, Project administration, Funding acquisition. **E. Geber:** Visualization, Validation, Methodology, Data curation.

#### Declaration of competing interest

The authors declare that they have no known competing financial interests or personal relationships that could have appeared to influence the work reported in this paper.

#### Data availability

Data will be made available on request.

## Acknowledgments

This project has received funding from the European Union's Horizon 2020 research and innovation program under the Marie Skłodowska-Curie projects No 861002 (EDEM) and No 101028449 (AI-FIE). This Article has been co-authored by National Technology and Engineering Solutions of Sandia, LLC. under contract No DE-NA0003525 with the U.S. Department of Energy/National Nuclear Security Administration. The United States Government retains and Elsevier, by accepting the article for publication, acknowledges that the United States Government retains a non-exclusive, paid-up, irrevocable, worldwide license to publish or reproduce the published form of this manuscript, or allow others to do so, for United States Government purposes.

## References

- [1] Anitescu G, Bruno TJ, Tavlarides LL. Dieseline for supercritical injection and combustion in compression-ignition engines: volatility, phase transitions, spray/jet structure, and thermal stability. *Energy Fuels* 2012;26(10):6247–58.
- [2] Arai Y, Sako T, Takebayashi Y. *Material Processing Using Supercritical Fluids. Supercritical Fluids: Molecular Interactions, Physical Properties, and New Applications*. 2002. p. 281–345.
- [3] Arcoumanis C, Gavaises M, French B. Effect of fuel injection processes on the structure of diesel sprays. *SAE Transactions*. 1997. p. 1025–64.
- [4] Bamgbade BA, et al. High-temperature, high-pressure volumetric properties of propane, squalane, and their mixtures: measurement and PC-SAFT modeling. *Ind Eng Chem Res* 2015;54(26):6804–11.
- [5] Baran O, et al. Assessment of injector-flow characteristics of additised and renewable diesel blends through high-speed imaging. *Fuel* 2023;352:129076.
- [6] M. Battistoni, "ECN7 - Diesel sprays: internal flow and near-field of Spray C & D," 2020. [Online]. Available: <https://ecn.sandia.gov/ecn-workshop/ecn7-workshop/>.
- [7] Battistoni M, Som S, Powell CF. Highly resolved Eulerian simulations of fuel spray transients in single and multi-hole injectors: nozzle flow and near-exit dynamics. *Fuel* 2019;251(November 2018):709–29. <https://doi.org/10.1016/j.fuel.2019.04.076>.
- [8] Beattie DRH, Whalley PB. Simple two-phase frictional pressure drop calculation method. *Int J Multiphase Flow*; (United Kingdom) 1982;8(1).
- [9] R. Bellini, C. Rodriguez, I.K. Karathanassis, and M. Gavaises, "Collapse of cavitation bubble clusters of fuels utilised with modern combustion systems," no. 2023.
- [10] Chapman WG, Gubbins KE, Jackson G, Radosz M. New reference equation of state for associating liquids. *Ind Eng Chem Res* 1990;29(8):1709–21. <https://doi.org/10.1021/ie00104a021>.
- [11] Cristofaro M, Edelbauer W, Koukouvinis P, Gavaises M. Large eddies simulation of the injector internal flow during a pilot injection. In: Proceedings of the 10th International Symposium on Cavitation (CAV2018); May 2018. [https://doi.org/10.1115/1.861851\\_ch127](https://doi.org/10.1115/1.861851_ch127).
- [12] Crua C, Manin J, Pickett LM. On the transcritical mixing of fuels at diesel engine conditions. *Fuel* 2017;208:535–48. <https://doi.org/10.1016/j.fuel.2017.06.091>.
- [13] Dahms RN, Oefelein JC. Liquid jet breakup regimes at supercritical pressures. *Combust Flame* 2015;162(10):3648–57.
- [14] Devassy BM, Edelbauer W, Greif D. Numerical simulation of the effect of 3D needle movement on cavitation and spray formation in a Diesel injector. In: *Journal of Physics: Conference Series*; 2015. p. 12092.
- [15] Dular M, Bachert B, Stoffel B, Sirok B. Relationship between cavitation structures and cavitation damage. *Wear* 2004;257(11):1176–84.
- [16] Espinoza DER, Scanlon TJ, Brown RE. Validation of tools to accelerate high-speed CFD simulations using openFOAM. In: 20th AIAA International Space Planes and Hypersonic Systems and Technologies Conference, 2015; 2015. p. 1–18. <https://doi.org/10.2514/6.2015-3566>.
- [17] ExxonMobil, "2023 Outlook for Energy," 2023.
- [18] Falgout Z, Rahm M, Sedarsky D, Linne M. Gas/fuel jet interfaces under high pressures and temperatures. *Fuel* 2016;168:14–21.
- [19] Fathi M, Hickel S. Rapid multi-component phase-split calculations using volume functions and reduction methods. *AIChE J* 2021;67(6):1–30. <https://doi.org/10.1002/aic.17174>.
- [20] Fathi M, Hickel S, Roekaerts D. Large eddy simulations of reacting and non-reacting transcritical fuel sprays using multiphase thermodynamics. *Phys Fluids* 2022;34(8). <https://doi.org/10.1063/5.0099154>.
- [21] Gavaises M, Murali-Girija M, Rodriguez C, Koukouvinis P, Gold M, Pearson R. Numerical simulation of fuel dribbling and nozzle wall wetting. *Int J Engine Res* 2022;23(1):132–49.
- [22] Geber E, et al. A general predictive methodology for fuel-mixture properties up to supercritical conditions. *Fluid Phase Equilib* 2023;574:113888. <https://doi.org/10.1016/j.fluid.2023.113888>.
- [23] Greenshields CJ, Weller HG, Gasparini L, Reese JM. Implementation of semi-discrete, non-staggered central schemes in a collocated, polyhedral, finite volume framework, for high-speed viscous flows. *Int J Numer Methods Fluids* 2009;38(2). <https://doi.org/10.1002/ld.2069>. p. n/a-n/a.
- [24] J. Gross and G. Sadowski, "Perturbed-Chain SAFT: an Equation of State Based on a Perturbation Theory for Chain Molecules," vol. 40, no. 4, pp. 1244–60, 2001, doi: 10.1021/ie0003887.
- [25] Gross J, Sadowski G. Application of the Perturbed-Chain SAFT Equation of State to Associating Systems. *Ind Eng Chem Res* 2002;41(22):5510–5. <https://doi.org/10.1021/ie010954d>.
- [26] Guo H, et al. Internal nozzle flow simulations of the ECN spray C injector under realistic operating conditions. *SAE Technical Papers* 2020;2020-April(April): 1–12. <https://doi.org/10.4271/2020-01-1154>.
- [27] Han Z, Uludogan A, Hampson GJ, Reitz RD. Mechanism of soot and NOx emission reduction using multiple-injection in a diesel engine. *SAE Transactions*. 1996. p. 837–52.
- [28] Harvey AH, Lemmon EW. Correlation for the second virial coefficient of water. *J Phys Chem Ref Data* 2004;33(1):369–76.
- [29] Hawi M, Kosaka H, Sato S, Nagasawa T, Elwardany A, Ahmed M. Effect of injection pressure and ambient density on spray characteristics of diesel and biodiesel surrogate fuels. *Fuel* 2019;254:115674.
- [30] Hopp M, Gross J. Thermal conductivity of real substances from excess entropy scaling using PC-SAFT. *Ind Eng Chem Res* 2017;56(15):4527–38. <https://doi.org/10.1021/acs.iecr.6b04289>.
- [31] Huang B, Ducoin A, Young YL. Physical and numerical investigation of cavitating flows around a pitching hydrofoil. *Phys. Fluids* 2013;25(10).
- [32] Huang SH, Radosz M. Equation of state for small, large, polydisperse, and associating molecules. *Ind Eng Chem Res* 1990;29(11):2284–94.
- [33] Huang SH, Radosz M. Equation of state for small, large, polydisperse, and associating molecules: extension to fluid mixtures. *Ind Eng Chem Res* 1991;30(8): 1994–2005.
- [34] Karathanassis IK, et al. X-ray phase contrast and absorption imaging for the quantification of transient cavitation in high-speed nozzle flows. *Phys Fluids* 2021;33(3). <https://doi.org/10.1063/5.0038475>.
- [35] Karathanassis IK, Trickett K, Koukouvinis P, Wang J, Barbour R, Gavaises M. Illustrating the effect of viscoelastic additives on cavitation and turbulence with X-ray imaging. *Sci Rep* 2018;8(1):14968.
- [36] Kook S, Pickett LM. Liquid length and vapor penetration of conventional, Fischer-Tropsch, coal-derived, and surrogate fuel sprays at high-temperature and high-pressure ambient conditions. *Fuel* 2012;93:539–48.
- [37] Koukouvinis P, Gavaises M, Li J, Wang L. Large Eddy Simulation of Diesel injector including cavitation effects and correlation to erosion damage. *Fuel* 2016. <https://doi.org/10.1016/j.fuel.2016.02.037>.
- [38] Koukouvinis P, Vidal-Roncero A, Rodriguez C, Gavaises M, Pickett L. High pressure/high temperature multiphase simulations of dodecane injection to nitrogen: application on ECN Spray-A. *Fuel* 2020;275:117871. <https://doi.org/10.1016/j.fuel.2020.117871>.
- [39] Kyriazis N, Koukouvinis P, Gavaises M. Numerical investigation of bubble dynamics using tabulated data. *Int J Multiphase Flow* 2017;93:158–77. <https://doi.org/10.1016/j.ijmultiphaseflow.2017.04.004>.
- [40] Lacaze G, Misdariis A, Ruiz A, Oefelein JC. Analysis of high-pressure diesel fuel injection processes using LES with real-fluid thermodynamics and transport. *Proc. Combust. Inst.* 2015;35(2):1603–11. <https://doi.org/10.1016/j.proci.2014.06.072>.
- [41] Leekumjorn S, Krejbjerg K. Phase behavior of reservoir fluids: comparisons of PC-SAFT and cubic EOS simulations. *Fluid Phase Equilib* 2013;359:17–23. <https://doi.org/10.1016/j.fluid.2013.07.007>.
- [42] Lemaire R, Faccinotto A, Therssen E, Ziskind M, Focsa C, Desgroux P. Experimental comparison of soot formation in turbulent flames of diesel and surrogate diesel fuels. *Proc. Combust. Inst.* 2009;32(1):737–44.
- [43] E.W. Lemmon, M.L. Huber, and M.O. McLinden, "NIST Standard Reference Database 23: reference Fluid Thermodynamic and Transport Properties-REFPROP, Version 9.1, National Institute of Standards and Technology," 2013, *Gaithersburg*.
- [44] Liang X, Maribo-Mogensen B, Thomsen K, Yan W, Kontogeorgis GM. Approach to improve speed of sound calculation within PC-SAFT framework. *Ind Eng Chem Res* 2012;51(45):14903–14. <https://doi.org/10.1021/ie3018127>.
- [45] Lin R. *Issues on Clean Diesel Combustion Technology Using Supercritical Fluids: Thermophysical Properties and Thermal Stability of Diesel Fuel*. Syracuse University; 2011.
- [46] Lin R, Tavlarides LL. Thermophysical properties needed for the development of the supercritical diesel combustion technology: evaluation of diesel fuel surrogate models. *J Supercritical Fluids* 2012;71:136–46. <https://doi.org/10.1016/j.supflu.2012.08.003>.
- [47] Liu F. A thorough description of how wall functions are implemented in OpenFOAM. In: *Proceedings of CFD with OpenSource Software*. 34; 2016.
- [48] Lötgering-Lin O, Gross J. Group Contribution method for viscosities based on entropy scaling using the perturbed-chain polar statistical associating fluid theory. *Ind Eng Chem Res* 2015;54(32):7942–52. <https://doi.org/10.1021/acs.iecr.5b01698>.
- [49] Ma PC, Wu H, Banuti DT, Ihme M. On the numerical behavior of diffuse-interface methods for transcritical real-fluids simulations. *Int J Multiphase Flow* 2019: 231–49. <https://doi.org/10.1016/j.ijmultiphaseflow.2019.01.015>.
- [50] Manin J, Pickett LM, Yasutomi K. Stereoscopic high-speed microscopy to understand transient internal flow processes in high-pressure nozzles. *Exp Therm Fluid Sci* 2020;114:110027.
- [51] J. Matheis and S. Hickel, "Multi-component vapor-liquid equilibrium model for LES and application to ECN Spray A," *arXiv preprint*, 2016.
- [52] Matheis J, Hickel S. Multi-component vapor-liquid equilibrium model for LES of high-pressure fuel injection and application to ECN Spray A. *Int J Multiphase*

- Flow 2018;99:294–311. <https://doi.org/10.1016/j.ijmultiphaseflow.2017.11.001>.
- [53] Michelsen ML. The isothermal flash problem. Part I. Stability. *Fluid Phase Equilib* 1982;9(1):1–19. [https://doi.org/10.1016/0378-3812\(82\)85001-2](https://doi.org/10.1016/0378-3812(82)85001-2).
- [54] Mitroglou N, Lorenzi M, Santini M, Gavaises M. Application of X-ray micro-computed tomography on high-speed cavitating diesel fuel flows. *Exp Fluids* 2016;57:1–14.
- [55] Mueller CJ, et al. Diesel surrogate fuels for engine testing and chemical-kinetic modeling: compositions and properties. *Energy & Fuels* 2016;30(2):1445–61.
- [56] Nicoud F, Ducros F. Subgrid-scale stress modelling based on the square of the velocity gradient tensor. *Flow Turbul Combust* 1999;62(3):183–200.
- [57] Nishida K, Zhu J, Leng X, He Z. Effects of micro-hole nozzle and ultra-high injection pressure on air entrainment, liquid penetration, flame lift-off and soot formation of diesel spray flame. *International Journal of Engine Research* 2017; 18(1–2):51–65.
- [58] J. Nocedal and S.J. Wright, “Numerical optimization 2nd edition springer,” *New York*, 2006.
- [59] A. Onorati et al., “The role of hydrogen for future internal combustion engines,” 2022, *SAGE Publications Sage UK: London, England*.
- [60] Orley F, Hickel S, Schmidt SJ, Adams NA. Large-eddy simulation of turbulent, cavitating fuel flow inside a 9-hole diesel injector including needle movement. *Int J Engine Res* 2017;18(3):195–211.
- [61] Orley F, Pasquariello V, Hickel S, Adams NA. Cut-element based immersed boundary method for moving geometries in compressible liquid flows with cavitation. *J Comput Phys* 2015;283:1–22.
- [62] Pickett LM, Siebers DL. Soot in diesel fuel jets: effects of ambient temperature, ambient density, and injection pressure. *Combust Flame* 2004;138(1–2):114–35.
- [63] Qiu L, Reitz RD. An investigation of thermodynamic states during high-pressure fuel injection using equilibrium thermodynamics. *Int J Multiphase Flow* 2015;72: 24–38.
- [64] R.D. Reitz et al., “IJER editorial: the future of the internal combustion engine,” 2020, *SAGE Publications Sage UK: London, England*.
- [65] Rodriguez C, Koukouvinis P, Gavaises M. Simulation of supercritical diesel jets using the PC-SAFT EoS. *J Supercrit Fluids* 2019;145:48–65. <https://doi.org/10.1016/j.supflu.2018.11.003>.
- [66] Rodriguez C, Rokni HB, Koukouvinis P, Gupta A, Gavaises M. Complex multicomponent real-fluid thermodynamic model for high-pressure Diesel fuel injection. *Fuel* 2019;257:115888. <https://doi.org/10.1016/j.fuel.2019.115888>.
- [67] Rodriguez C, Vidal A, Koukouvinis P, Gavaises M, McHugh MA. Simulation of transcritical fluid jets using the PC-SAFT EoS. *J Comput Phys* 2018;374(July): 444–68. <https://doi.org/10.1016/j.jcp.2018.07.030>.
- [68] Rodriguez C, Vidal A, Koukouvinis P, Gavaises M, McHugh MA. Simulation of transcritical fluid jets using the PC-SAFT EoS. *J Comput Phys* 2018;374:444–68. <https://doi.org/10.1016/j.jcp.2018.07.030>.
- [69] Rokni HB, Gupta A, Moore JD, McHugh MA, Bamgbade BA, Gavaises M. Purely predictive method for density, compressibility, and expansivity for hydrocarbon mixtures and diesel and jet fuels up to high temperatures and pressures. *Fuel* 2019;236(August 2018):1377–90. <https://doi.org/10.1016/j.fuel.2018.09.041>.
- [70] Rosenfeld Y. Relation between the transport coefficients and the internal entropy of simple systems. *Phys Rev A (Coll Park)* 1977;15(6):2545.
- [71] Rowane AJ, Gupta A, Gavaises M, McHugh MA. Experimental and modeling investigations of the phase behavior and densities of diesel + nitrogen mixtures. *Fuel* 2020;265. <https://doi.org/10.1016/j.fuel.2020.117027>.
- [72] Salimi M, Bahramian A. The prediction of the speed of sound in hydrocarbon liquids and gases: the peng-robinson equation of state versus SAFT-BACK. *Pet Sci Technol* 2014;32(4):409–17. <https://doi.org/10.1080/10916466.2011.580301>.
- [73] Salvador FJ, Martínez-López J, Romero JV, Roselló MD. Computational study of the cavitation phenomenon and its interaction with the turbulence developed in diesel injector nozzles by Large Eddy Simulation (LES). *Math Comput Model* 2013;57(7–8):1656–62.
- [74] Sandia National Laboratories, “Spray A.” [Online]. Available: <https://ecn.sandia.gov/diesel-spray-combustion/target-condition/spray-ab/>.
- [75] Sandia National Laboratories, “Spray C Nozzle Geometry.” Accessed: Jun. 30, 2023. [Online]. Available: <https://ecn.sandia.gov/diesel-spray-combustion/target-condition/spray-c-nozzle-geometry/>.
- [76] Sandia National Laboratories, “Spray C Nozzle Geometry.” [Online]. Available: <https://ecn.sandia.gov/diesel-spray-combustion/target-condition/spray-c-nozzle-geometry/>.
- [77] Santos EG, Shi J, Gavaises M, Soteriou C, Winterbourn M, Bauer W. Investigation of cavitation and air entrainment during pilot injection in real-size multi-hole diesel nozzles. *Fuel* 2020;263:116746.
- [78] Santos EG, Shi J, Gavaises M, Soteriou C, Winterbourn M, Bauer W. Investigation of cavitation and air entrainment during pilot injection in real-size multi-hole diesel nozzles. *Fuel* 2020;263:116746.
- [79] R.B. Schnabel and E. Eskow, “A Revised Modified Cholesky Factorization Algorithm 1”.
- [80] E. Scientific, P. Company, and L. Michelsen, “The isothermal flash problem. part ii. phase-split calculation,” vol. 9, 1982.
- [81] Sforzo BA, et al. Fuel Nozzle Geometry Effects on Cavitation and Spray Behavior at Diesel Engine Conditions. In: *Proceedings of the 10th International Symposium on Cavitation (CAV2018)*; 2019. p. 474–80. [https://doi.org/10.1115/1.861851\\_ch90](https://doi.org/10.1115/1.861851_ch90).
- [82] Sforzo BA, et al. Fuel Nozzle Geometry Effects on Cavitation and Spray Behavior at Diesel Engine Conditions. In: *Proceedings of the 10th International Symposium on Cavitation (CAV2018)*; 2019. p. 474–80. [https://doi.org/10.1115/1.861851\\_ch90](https://doi.org/10.1115/1.861851_ch90).
- [83] Sou A, Hosokawa S, Tomiyama A. Effects of cavitation in a nozzle on liquid jet atomization. *Int J Heat Mass Transf* 2007;50(17–18):3575–82.
- [84] Spiteri RJ, Ruuth SJ. A New Class of Optimal High-Order Strong-Stability-Preserving Time Discretization Methods. *SIAM J Numer Anal* 2002;40(2):469–91. <https://doi.org/10.1137/S0036142901389025>.
- [85] Stavropoulos Vasilakis E, Rodriguez C, Kyriazis N, Malgarinos I, Koukouvinis P, Gavaises M. A direct forcing immersed boundary method for cavitating flows. *Int J Numer Methods Fluids* 2021;93(10):3092–130. <https://doi.org/10.1002/fld.5026>.
- [86] Stavrou M, Bardow A, Gross J. Estimation of the binary interaction parameter kij of the PC-SAFT Equation of State based on pure component parameters using a QSPR method. *Fluid Phase Equilib* 2016;416:138–49.
- [87] Strotos G, et al. Fuel heating in high pressure diesel nozzles. In: *International Conference Thiesel*; 2014.
- [88] Tekawade A, Sforzo BA, Matusik KE, Fezzaa K, Kastengren AL, Powell CF. Time-resolved 3D imaging of two-phase fluid flow inside a steel fuel injector using synchrotron X-ray tomography. *Sci Rep* 2020;10(1):1–9. <https://doi.org/10.1038/s41598-020-65701-x>.
- [89] Tihic A, Kontogeorgis GM, von Solms N, Michelsen ML, Constantinou L. A Predictive Group-Contribution Simplified PC-SAFT Equation of State: application to Polymer Systems. *Ind Eng Chem Res* 2008;47(15):5092–101. <https://doi.org/10.1021/ie0710768>.
- [90] Torelli R, et al. Evaluation of shot-to-shot in-nozzle flow variations in a heavy-duty diesel injector using real nozzle geometry. *SAE Int J Fuels Lubr* 2018;11(4): 379–96.
- [91] Toro EF. No Title. *Angewandte Chemie Int Ed* 2001;40(6):9823. [https://doi.org/10.1002/1521-3773\(20010316\)40:6<9823::AID-ANIE9823>3.3.CO;2-C](https://doi.org/10.1002/1521-3773(20010316)40:6<9823::AID-ANIE9823>3.3.CO;2-C).
- [92] Tumakaka F, Sadowski G. Application of the Perturbed-Chain SAFT equation of state to polar systems. *Fluid Phase Equilib* 2004;217(2):233–9.
- [93] M.G.J. Vaz et al., “Numerical Simulation of Multicomponent Diesel Fuel Spray Surrogates Using Real-Fluid Thermodynamic Modelling,” 2022.
- [94] Vera-Tudela W, Haefeli R, Barro C, Schneider B, Boulouchos K. An experimental study of a very high-pressure diesel injector (up to 5000 bar) by means of optical diagnostics. *Fuel* 2020;275:117933.
- [95] Vidal A, Kolovos K, Gold MR, Pearson RJ, Koukouvinis P, Gavaises M. Preferential cavitation and friction-induced heating of multi-component Diesel fuel surrogates up to 450MPa. *Int J Heat Mass Transf* 2021;166:120744.
- [96] Vidal A, Koukouvinis P, Gavaises M. Vapor-liquid equilibrium calculations at specified composition, density and temperature with the perturbed chain statistical associating fluid theory (PC-SAFT) equation of state. *Fluid Phase Equilib* 2020;521:112661. <https://doi.org/10.1016/j.fluid.2020.112661>.
- [97] Vidal A, Koukouvinis P, Gavaises M. Vapor-liquid equilibrium calculations at specified composition, density and temperature with the perturbed chain statistical associating fluid theory (PC-SAFT) equation of state. *Fluid Phase Equilib* 2020;521:112661. <https://doi.org/10.1016/j.fluid.2020.112661>.
- [98] Vidal A, Rodriguez C, Koukouvinis P, Gavaises M, McHugh MA. Modelling of diesel fuel properties through its surrogates using perturbed-chain, statistical associating fluid theory. *Int J Engine Res* 2018;146808741880171. <https://doi.org/10.1177/1468087418801712>.
- [99] Wilson GM. A modified Redlich-Kwong equation of state, application to general physical data calculations. In: *65th National AIChE Meeting*; 1969.
- [100] Wu Y, et al. Experimental measurements and equation of state modeling of liquid densities for long-chain n-alkanes at pressures to 265 MPa and temperatures to 523 K. *Fluid Phase Equilib* 2011;311:17–24.
- [101] Zhang L, He Z, Guan W, Wang Q, Som S. Simulations on the cavitating flow and corresponding risk of erosion in diesel injector nozzles with double array holes. *Int J Heat Mass Transf* 2018;124:900–11.
- [102] Zhao H, et al. Validation of a three-dimensional internal nozzle flow model including automatic mesh generation and cavitation effects. *J Eng Gas Turbine Power* 2014;136(9):92603.